Concentration and Velocity Profiles in a Polymeric Lithium-ion Battery Electrolyte

1   Title:
2   *Concentration and Velocity Profiles in a Polymeric Lithium-ion Battery Electrolyte*
3
4   Authorship:
5   Hans-Georg Steinrück,[1,2,3,*,+] Christopher J. Takacs,[1,2,*,+] Hong-Keun Kim,[4,5] David M. Mackanic,[6] Benjamin
6   Holladay,[7] Chuntian Cao,[1] Suresh Narayanan,[8] Eric M. Dufresne,[8] Yuriy Chushkin,[9] Beatrice Ruta,[9,10]
7   Federico Zontone,[9] Johannes Will,[11] Oleg Borodin,[12] Sunil K. Sinha,[7] Venkat Srinivasan,[4,5] and Michael F.
8   Toney[1,2,13,*]
9
10   [1]SSRL Materials Science Division, SLAC National Accelerator Laboratory, Menlo Park, California 94025,
11   USA
12   [2]SLAC National Accelerator Laboratory, Joint Center for Energy Storage Research (JCESR), Lemont, Illinois
13   60439, USA
14   [3]Department Chemie, Universität Paderborn, 33098 Paderborn, Germany
15   [4]Argonne National Laboratory, Lemont, Illinois 60439, USA
16   [5]Argonne National Laboratory, Joint Center for Energy Storage Research (JCESR), Menlo Park, California
17   94025, USA
18   [6]Department of Chemical Engineering, Stanford University, Stanford, California 94305, USA
19   [7]Department of Physics, University of California, San Diego, La Jolla, California 92093-0319, USA
20   [8]X-ray Science Division, Argonne National Laboratory, Lemont, Illinois 60439, USA
21   [9]ESRF – The European Synchrotron, 71 avenue des Martyrs, 38043 Grenoble, France
22   [10]Universté Lyon, Universitè Claude Bernard Lyon 1, CNRS, Institut Lumière Matière, Villeurbanne, France.
23   [11]Institute of Micro- and Nanostructure Research (IMN) & Center for Nanoanalysis and Electron
24   Microscopy (CENEM), University of Erlangen-Nuremberg, Germany
25   [12]Energy Storage Branch, Sensor and Electron Devices Directorate, U.S. Army Research Laboratory,
26   Adelphi, MD 20783, USA
27   [13]Department of Chemical and Biological Engineering, University of Colorado, Boulder, CO 80309, USA
28
29   *: hans.georg.steinrueck@uni-paderborn.de, ctakacs@slac.stanford.edu, michael.toney@colorado.edu
30   +: Equal contribution
31
32   *Author contributions*: Conceptualization: HGS, CJT, HHK, DMM, BH, OB, SKS, VS, MFT. Methodology: HGS,
33   CJT, HHK, DMM, BH, OB, SKS, VS, MFT. Software: HGS, CJT, HHK, DMM, BH, OB. Validation: HGS, CJT, HHK,
34   DMM, BH, CC, SN, EMD, YC, BR, FZ, JW, OB, SKS, VS, MFT. Formal analysis: HGS, CJT, HHK, DMM, BH, OB.
35   Investigation: HGS, CJT, HHK, DMM, BH, CC, SN, EMD, YC, BR, FZ, JW, OB, SKS, VS, MFT. Resources: HGS,
36   CJT, HHK, DMM, BH, CC, SN, EMD, YC, BR, FZ, JW, OB. Data Curation: HGS, CJT, HHK, DMM, BH, OB. Writing
37   – original draft preparation: HGS, CJT, HHK, DMM, OB. Writing – review and editing: HGS, CJT, HHK, DMM,
38   BH, CC, SN, EMD, YC, BR, FZ, JW, OB, SKS, VS, MFT. Visualization: HGS, OB. Supervision: HGS, CJT, OB, SKS,
39   VS, MFT. Project administration: HGS, CJT, DMM. Funding acquisition: SKS, OB, VS, MFT.

40   **Abstract**:

41   Predictive knowledge of ion transport in electrolytes which bridges microscopic and macroscopic length

42   scales is imperative to design new ion conductors and to simulate device performance. Here, we employed

43   a novel approach combining *operando* X-ray photon correlation spectroscopy, X-ray absorption microscopy,

44   continuum modelling, and molecular dynamics simulations to probe ion transport in a baseline polymeric

45   lithium-ion battery electrolyte. In a Li/PEO-LiTFSI/Li symmetric cell under polarization, we determined and

46   rationalized microscopic properties including local electrolyte velocities and ion correlations and connected

47   this insight to measured and simulated macroscopic ion concentration gradients. By relating our results

48   across length scales, we suggest a fairly concentration-independent transference number of about 0.2. Our

49   study shows the broad applicability of *operando* X-ray photon correlation spectroscopy to the

50   understanding of dynamic phenomena.

Introduction

Understanding ion transport is of fundamental importance in natural sciences and engineering. Examples include biological ion pumps for life processes [1, 2], porous membranes for separations [3, 4], and electrodes and electrolytes in diverse electrochemical systems [5, 6]. While continuum level models can be used to predict macroscopic transport related behavior, the link to the microscopic transport mechanism is still to be realized [7]. Connecting the corresponding spatial and temporal scales is hence a major goal towards quantitatively predicting how ions navigate through natural and designed systems. Electrochemical energy storage is one field where ions transport from one electrode to another through an electrolyte and is societally important towards the goal of carbon neutrality. Hence, knowledge of transport phenomena is necessary to both design new electrolyte and electrode materials and to accurately simulate the performance and safety of an electrochemical cell. This requires knowledge of the temperature- and ion concentration-dependent transport properties of an electrolyte, including thermodynamic mean salt molal activity coefficient, conductivity (σ), salt diffusion coefficient (D), and the cation transference number (t^+) [8, 9]. The transference number is defined as the ratio of current carried by the cation to the total electric current, and is related to mobilities of anion and cation in dilute solutions and Stefan-Maxwell diffusion coefficients in concentrated solutions [10]. Importantly, these macroscopic quantities are intimately related to atomistic diffusion mechanisms [5, 11-14]. For accurate cell simulations, the transport coefficients σ, D, and t^+ must be known with high accuracy from experimental measurements, which is often complicated and necessitates many assumptions. Here, we present a novel approach in which we combine local *operando* measurements of electrolyte velocities and global measurements of ion concentrations with molecular scale simulations and continuum level modelling to relate molecular transport mechanisms with macroscopically observed transport phenomena. We anticipate that our method can be extended towards a variety of ion conducting materials.

The system we investigated is a polymer electrolyte for lithium-ion batteries (LIBs). Polymer electrolytes are a safe alternative to commonly used flammable liquid organic electrolytes [5, 15, 16]. However, their wide-spread adoption is hampered by typically poor ion transport properties. While the relevance of the transference number is sometimes overlooked [17], its importance in polymer electrolyte for LIBs with regards to energy and power density was recognized in the early 1990s by Doyle, Fuller and Newman [18]. The consequence of a transference number deviating from unity is concentration polarization, which has strong impact on LIB performance. A simple example is a Li/electrolyte/Li cell (anion blocking) under constant voltage conditions. Here, concentration polarization corresponds to a continued piling-up of anions and cations at the stripping electrode, and concurrent depletion near the plating side. Steady state is reached when the net motion of anions reaches zero which is the condition that the diffusion force acting on anions due to the concentration gradient is equal to the migration force from the electric field (in the absence of convection). At high concentrations, volume conservation has the additional consequence of solvent mass transport upon salt mass transport [19]. A conceptualization of mass transport phenomena occurring during polarization of a Li/electrolyte/Li symmetric cell is shown in **Figure 1**(a)**.** The concentration polarization is easily observed as the decrease in current upon constant voltage cell polarization until a steady-state current is reached [20]. This increase in electrolyte resistance for ion conductors with non-unity transference number ultimately limits batteries' achievable rates, critical currents, and cutoff voltages (due to overpotentials), reducing the usable energy and power density. Hence, the transference number is an

94 essential descriptor of ion transport. Nevertheless, researchers still argue about transference number
95 values, even in baseline systems such as lithium bistrifluoromethanesulfonimidate (LiTFSI) in Poly(ethylene
96 oxide) (PEO) [21]. The transference number can be measured via the steady-state Bruce-Vincent polarization
97 method [22, 23], the Balsara-Newman method [24], as well as pulsed field gradients NMR (pfg-NMR) [25] and pulsed
98 field gradients electrophoretic NMR (e-NMR) [21]. Despite extensive efforts towards unified results of these
99 approaches, in particular as a function of ion concentration, a clear picture has not yet emerged.
100
101 Towards this end, we developed an alternative approach towards determining the ion transport
102 properties. Specifically, we directly and *operando* measured precise microscopic and macroscopic physical
103 properties of the electrolyte upon cell polarization in a Li/electrolyte/Li cell, combined this with calculations
104 via concentrated solution theory continuum modelling (CM), and rationalized our findings with microscopic
105 insight from molecular dynamics (MD) simulations. We utilized a well-studied benchmark model system
106 electrolyte consisting of PEO and LiTFSI at Li$^+$ to EO molar ratio of r = 0.1. Under constant voltage
107 polarization, we directly measured the velocity associated with electrolyte and ions via heterodyne
108 synchrotron X-ray photon correlation spectroscopy (XPCS), and the TFSI$^-$ concentration gradient from
109 electrode to electrode via X-ray absorption microscopy (XAM). This novel approach is conceptualized in
110 **Figure 1**(b). The significance of our results lies in the unification of microscopic and macroscopic predictions
111 from simulation with experimental measurements as well as the self-consistent determination of a
112 concentration-independent transference numbers of approximately 0.2. Our study paves the way for
113 further length- and time-scale bridging understanding of ion transport.
114
115
116 **Experimental: Approach – experimental and modeling velocity and concentration profiles**
117
118 The electrolyte velocity measurements were conducted using XPCS [26, 27] in heterodyne modality, [28-31] as
119 illustrated in **Figure 1**(b). XPCS measures the time evolution of the coherent scattering pattern (speckle
120 pattern), which encodes sample dynamics. In heterodyne XPCS, a static reference scattering signal is mixed
121 with the dynamic scattering signal of the polymer electrolyte (details in *Supporting Information*). The
122 resultant phase shift in the coherent scattering due to the constant velocity motion of the sample with
123 respect to a fixed reference yields oscillations in the auto-correlation function $g_2(\mathbf{q}, \tau)$, which correlates
124 the intensity in a given pixel at time t to that at $t + \tau$; here, $\mathbf{q}$ is the scattering vector and τ is the delay
125 time. The heterodyne auto-correlation function with heterodyne fraction h and sample velocity vector $\mathbf{v}$ is
126 given by

$$g_2(\mathbf{q},\tau) = 1 + \beta(1-h)^2 + h^2\beta e^{-2\left(\frac{\tau}{\tau_0(q)}\right)^\gamma} + 2h(1-h)\beta \cos\omega\tau\, e^{-\left(\frac{\tau}{\tau_0(q)}\right)^\gamma}$$

Equation 1

129 with

$$\omega = \mathbf{q}.\mathbf{v} = qv\cos\chi.$$

Equation 2

132 Here χ is the angle between scattering and velocity vector [28, 32], β is the coherence factor, and τ_0 is systems
133 relaxation time. The relaxation is modelled by a stretched exponential decay with stretching factor γ.
134 Equation 2 allows for the rescaling and collapse of all correlation functions as functions of $\mathbf{q}$ and τ into a
135 single master curve as shown in Figure 2. **Figure 2**(a) shows 18 χ-dependent correlation functions at a single

136   q and the corresponding fits to Equation 1; these data were obtained at beamline 8-ID-I at the Advanced
137   Photon Source. The $\cos\chi$-dependence of the derived oscillation frequencies ω is shown in **Figure 2**(c)
138   together with a fit to Equation 2. The agreement between data and model allows us to calculate χ-scaled
139   correlation functions at each q, which are shown in **Figure 2**(b) together with fits to Equation 1. The q-
140   dependence of the derived ω is shown in **Figure 2**(d). The observed linearity allows us to apply an additional
141   linear q-scaling, yielding a single global master q- and χ-scaled correlation function (**Figure 2**(e)), which
142   shows oscillations, the inverse period of which corresponds to the velocity (details in ***Supporting***
143   ***Information***).

144

145   Electrolyte velocities were measured *operando* during approximately 1000 minutes of polarization of
146   a Li/PEO-LiTFSI/Li symmetric cell at a constant voltage of 0.3 V at 90°C using a specially designed cell with
147   the electrodes separated by 3 mm (details in ***Supporting Information***). Position sensitivity was achieved by
148   utilizing a 15 µm X-ray beam positioned at different locations across the channel. In addition, during the
149   same polarization experiment, XAM was utilized to measure the TFSI$^-$ ion concentration gradient across the
150   channel. For this purpose, the sample was raster-scanned across the channel, and the transmitted X-ray
151   intensity was recorded, which was related to the concentration via Lambert-Beer's law making use of the
152   significantly higher absorption cross section for TFSI$^-$ compared to PEO (details in ***Supporting Information***).
153   The velocity and concentration gradients were then compared to our continuum modelling, where we
154   employed concentrated solution theory, a mathematical one-dimensional model by Newman [9] with a
155   macro-homogenous assumption of the electrolyte (details in ***Supporting Information***). These macroscopic
156   insights into the transport phenomena were coupled to the microscopic insights from MD simulations
157   employing the Wohde-Roling-formalism [33].

158

159   To compare our measured concentration gradients and electrolyte velocities to those predicted by CM,
160   we chose two transport coefficients from recent literature. The first set (denoted ***RS transport coefficients***)
161   corresponds to values obtained by Rosenwinkel/Schönhoff [21] via the model-free approach of measuring
162   the electrophoretic mobilities of the ions via e-NMR. The second (denoted ***PNB transport coefficients***)
163   corresponds to values obtained by Pesko et al. [25, 34] via the Balsara-Newman method. We note in passing
164   that the former method yields similar values as obtained via Bruce-Vincent method and pfg-NMR [21, 25, 35, 36].
165   The rationale behind our choice lies in the large differences in the transference number of ***RS transport***
166   ***coefficients*** and ***PNB transport coefficients*** close to r = 0.1, making our approach particularly sensitive to
167   providing insight into the controversy regarding transference numbers around r = 0.1. We point out that
168   the effective transference numbers used in the calculations vary with time and position due to their
169   concentration dependence (concentration changes by ~ 50% upon several hours of polarization);
170   accordingly, we effectively probe a large range of concentrations from about r = 0.04 to r = 0.16, even
171   though we studied only a single starting concentration. This variation is insignificant in the case of ***RS***
172   ***transport coefficients***, whereas it is significant in the case of ***PNB transport coefficients***. The exact transport
173   coefficients used in our calculations are tabulated in **Table S3**. As the referenced studies were performed
174   in the conductive temperature-regime of PEO-LiTFSI at 90°C, above its glass transition and melting
175   temperature[15], we also chose 90°C.

176

177

178

179   Results and Discussion

180

181   **Figure 3**(a) shows the experimentally measured current density (black line) upon 0.3 V polarization and the
182   corresponding prediction from CM using input *RS transport coefficients* (blue line) and *PNB transport*
183   *coefficients* (red line). The overall shape of the curve is well reproduced by the model calculations. A more
184   detailed comparison is illustrated in **Figure 3**(b) where the ratios between the predicted and measured
185   current densities are plotted. Measurements and prediction are within 10% over the entire polarization
186   time independent of the model. While there are subtle shape changes during the first approximately 200
187   minutes, both predictions have a fairly constant difference from the measurement. We note that for an
188   exact comparison, the interfacial resistance (e.g. due to nm-scale interfacial film formation upon TFSI[-]
189   reduction[37-40]) would need to be subtracted; it can be expected that bulk contributions are, however,
190   dominant given the 3 mm channel thickness[25]. Nevertheless, it is apparent that a comparison of the current
191   densities alone does not allow for distinguishing between the two chosen transport coefficient models,
192   even though the transference numbers are vastly different (see **Table S3**). To compare these two
193   parameter-sets more rigorously and sensitively, we now examine the measured concentration polarization
194   (via XAM) and ion velocities (via XPCS) to those predicted by CM. We note that the XAM was inspired by
195   optical methods of determining ion concentrations [41-45] and quantitative determination of ion
196   concentration gradients using x-ray phase contrast imaging [46].

197

198   The XAM-derived concentration profiles (markers) upon cell polarization at 0.3 V are shown in **Figure**
199   **4**(a) and (b) together with the profiles derived from CM (solid lines) (see **Figure S9** for false-color plot of
200   time-position dependence); these XAM data were obtained at beamline 8-ID-I at the Advanced Photon
201   Source. **Figure 4**(a) corresponds to simulation results using *RS transport coefficients*, whereas (b)
202   corresponds to *PNB transport coefficients*. The experimental profiles (symbols in (a) and (b)) are symmetric,
203   with the concentration gradient centered on the cell center. The concentration gradients predicted using
204   *RS transport coefficients* (**Figure 4**(a)) also show a symmetric profile that is centered close to the cell center,
205   and hence matches the experimental data. On the contrary, the concentration gradients predicted using
206   *PNB transport coefficients* (**Figure 4**(b)) exhibit asymmetric profiles that are not centered on the cell center.
207   Qualitatively, this asymmetry results from sharply varying transference numbers in a narrow concentration
208   regime near r = 0.1 (see **Table S3**). We note that since the TFSI[-] concentration changes by > 30% in our
209   experiment, we are able to effectively probe the transference numbers over a wide range of salt-to-
210   polymer concentrations, which is an advantage compared to single concentrations measurements. An
211   overlay plot of the concentration gradient highlighting the observed behavior in **Figure 4** between
212   experiment and the two predictions at t = 707 mins is shown in **Figure S10** in the *Supporting Information*.

213

214   Next, we first discuss the origin of the XPCS-measured velocity and then discuss our observations with
215   respect to the CM predictions. Specifically, this velocity corresponds to the relative velocity of the part of
216   the sample that gives rise to the scattering in the measured q-range with respect to the static cell windows;
217   this is essentially equivalent to referencing the velocity with respect to the lithium electrodes, as these are
218   rigidly clamped to the windows and static (see **Figure S11**).

219

220   The measured q-range was between $q_{min} = 0.0029 \, \text{Å}^{-1}$ and $q_{max} = 0.0192 \, \text{Å}^{-1}$ (see *Supporting*
221   *Information*), i.e. the scattering in the measured range originates from density fluctuations on length scales

222   of $2\pi/q \approx 300 - 2000\,\text{Å}$. Intuitively, this suggests that the observed scattering has its origin in
223   heterogeneities in the network structure of the polymer-LiTFSI melt, rather than in the individual TFSI⁻
224   anions, which have a size of less than $10\,\text{Å}$. This is consistent with the measured scattering intensity as a
225   function of time. **Figure S3** shows the transmission corrected mean scattering intensity as a function of time
226   for the five different locations, normalized to the initial mean intensity, and **Figure S4** shows $I(q)$ for several
227   locations over time. We observe a trend in which the scattering intensity increases for decreasing ion
228   concentration, whereas the scattering intensity decreases for increasing ion concentration. In the center
229   of the channel, where the ion concentration essentially remains unchanged, the scattering intensity also
230   does not vary significantly. This demonstrates that XPCS originates from the dynamics of the density
231   fluctuations in the arrangement of polymer chains and that the measured velocity corresponds to the
232   motion of the overall polymer-salt matrix with respect to the electrodes.

234   Interestingly, the structural properties of the LiTFSI/PEO network evolve faster during ionic mass
235   transport compared to equilibrium conditions at open circuit before polarization. This is evident from **Figure
236   S12**, which shows auto-correlation functions before and after cell polarization. The decay time (τ_0 in
237   **Equation 2**) before polarization is about one order of magnitude slower and exhibits no χ-dependence, as
238   expected. Since the decay time encodes the system's self-dynamics and is in principle independent of any
239   velocity field [28], these observations suggest that the moving ions disrupt the polymer network, resulting in
240   rearrangements of the network on time-scales faster than the self-dynamics at open circuit equilibrium.
241   While the dynamics slow down during polarization, it is unclear if the altered dynamics are a result of
242   motion of the cation or of the anion or both as steady state was not reached (during which only cation
243   contributions would be observed).

245   On a macroscopic level, a combination of volume conservation, local and global incompressibility of
246   the polymer, and electroneutrality imposes that the anion velocity is related to the solvent velocity via [19]

$$v_{\text{TFSI}^-} = -\varepsilon v_{\text{EO}},$$

248   **Equation 3**

249   where $\varepsilon = \dfrac{V_{\text{EO}}c_{\text{EO}}}{V_{\text{LiTFSI}}c_{\text{LiTFSI}}}$, and c_{EO} and c_{TFSI} are the concentration of solvent and salt, respectively, and V_{EO}
250   and V_{TFSI} are the molar volumes of solvent and salt, respectively. In other words, the polymer needs to
251   "make space" for TFSI⁻ ions that would like to pile up near the positive terminal. A microscopic illustration
252   of this phenomenon is shown in the *Supporting Information* (**Figure S13**).

254   Since the CM predicts the TFSI⁻ velocity and XPCS measures the ensemble average velocity of EO
255   monomers, to relate these, we now need to estimate the molar volumes of EO monomers and LiTFSI salt.
256   Assuming that molar volumes are independent of concentration, the individual solvent and salt molar
257   volumes can be determined by fitting the concentration dependence of the mass density [47] for the molar
258   ratio r to

$$\rho = \frac{M_{\text{LiTFSI}}+(M_{\text{EO}}/r)}{V_{\text{LiTFSI}}+(V_{\text{EO}}/r)},$$

260   **Equation 4**

261   where M_{EO} and M_{LiTFSI} are the molar masses of the EO monomer and LiTFSI of 44.05 and 287.08 g/mol,
262   respectively. The density data by Pesko et al. [25] is shown together with the fit in **Figure S14**, yielding molar
263   volume derived molecular volumes of $V_{\text{EO}}^{\text{molecule}} = 66.4 \pm 0.73\,\text{Å}^3$ and $V_{\text{TFSI}}^{\text{molecule}} = 224 \pm 7\,\text{Å}^3$, values in

264   good agreement with the numbers obtained for EO from the PEO density of 65 Å^3, and for the volume of
265   TFSI of 248 Å^3 [48]. Accordingly, for $r = 0.1$ we find $\varepsilon = -(2.95 \pm -0.01)$. This means that the XPCS
266   measured velocity (of the EO ensemble average) must be multiplied by 2.95 to yield a velocity for TFSI⁻. We
267   point out that assuming a constant ratio is an approximation since the ion concentration changes as a
268   function of x, and thus r, which would affect the conversion factor, and since there is the potential
269   existence of ion clustering,[49, 50] which is not taken into account in this conversion. Since the CM predicted
270   TFSI⁻ velocity is referenced with respect to the solvent velocity [9], it overestimates the velocity with respect
271   to the fixed electrodes. This is accounted by the conversion factor $\kappa = \frac{1}{\varepsilon} + 1$ for the TFSI- velocity derived
272   from XPCS for a direct comparison with the anion velocities from CM. This highlight the importance of
273   accounting for the solvent velocity when comparing predictions from concentrated solution theory to
274   precision measurements.
275
276   Comparisons between the XPCS determined TFSI⁻ velocities upon 0.3 V cell polarization, and those
277   predicted from CM using *RS transport coefficients* and *PNB transport coefficients* are shown in **Figure 5**.
278   Specifically, the velocities are shown for five different locations across the channel. While the overall
279   predicted curves exhibit similar profiles and resemble the shape of the electrochemically measured current
280   density, substantial differences can be observed in the evolution of the velocities over time at the different
281   positions. Specifically, experimental and both simulated velocity profiles show three regimes. We,
282   somewhat arbitrarily, break them down into a "slow" (e.g. experimental velocity < 50 Å/s at t = 300 min),
283   "medium" (e.g. experimental velocity < 100 Å/s at t = 300 min), and "fast" (e.g. experimental velocity > 100
284   Å/s at t = 300 min) TFSI⁻ velocity regimes; however, these are differently distributed across the cell
285   depending on the transport model: for *RS transport coefficients, the* yellow and green location belong to
286   the fast regime, blue and black location to the medium regime, and the magenta to the slow regime. On
287   the contrary, for *PNB transport coefficients*, the green, yellow, and blue location belong to the fast regime,
288   the black location to the medium regime, and the magenta to the slow regime. The experimental spatial
289   velocity variation along cell length (x) resembles the one simulated using *RS transport coefficients*, whereas
290   substantial differences are observed for *PNB transport coefficients.* This is manifested by the fact that the
291   variation in difference between simulation and experiment shows significantly less spread across the
292   different positions for the CM calculations using the *RS transport coefficients* as compared to the *PNB*
293   *transport coefficients* (see **Figure S16**). This is illustrated in the inset of **Figure 5**(a), which shows the
294   polarization time-averaged ratio of the XPCS determined TFSI⁻ velocity and those obtained using CM. While
295   there is an absolute difference between the measured and predicted velocities in both cases and the
296   magenta location appears to be an outlier, (see also **Figure S15** and **Figure S16**), the position dependence
297   shows a better match to the profiles calculated using *RS transport coefficients*, as evident from the fact that
298   the black, yellow, green, and blue location exhibit ratios falling within the red bar in the inset of **Figure 5**(a),
299   whereas only the yellow and green location fall within this range for the *PNB transport coefficients* (see also
300   **Figure S17**). This is quantified by a standard deviation of the ratio at the black, yellow, green, and blue
301   location of 0.08 for *RS transport coefficients* and 0.12 for *PNB transport coefficients.* Together with the
302   results of the XAM and MD simulations below (Fig. 4), our velocity measurement results support the *RS*
303   *transport coefficients.*
304
305   To provide a mechanistic microscopic rationalization of both microscopic velocities measurements
306   and macroscopic concentration polarization discussed above, we employed MD simulations (simulation

307 box snapshot in Figure S7a) at temperatures of 90 - 150 °C that predict structural and transport properties
308 in good agreement with experiments (**Figures S7b and S8**). Specifically, we analyze t^+_{app}, which is the
309 apparent transference number that does not explicitly include ion-ion correlations and is extracted from
310 self-diffusion coefficients and corresponds to pfg-NMR results, as well as t^+, which includes ionic
311 correlations to the flux under anion blocking conditions. The latter is extracted via application of Onsager
312 reciprocal relations combined with linear response theory within the Wohde-Roling-formalism [33] and is
313 comparable to e-NMR results (see **Equations S22 - 26** in *Supporting Information*). For r = 0.1, our MD
314 simulations predict t^+_{app} = 0.17 - 0.20, whereas a smaller value is found for t^+ = 0.12-0.13. Both of these
315 predictions are within experimental error bars reported from pfg-NMR and e-NMR (*RS transport*
316 *coefficients*) by Rosenwinkel et al. [21]. At higher salt concentration of r = 0.16, MD simulations predict t^+ =
317 0.17 − 0.20, which suggest fairly concentration-independent transference numbers around 0.2 consistent
318 with *RS transport coefficients,* supporting our experimental findings. To rationalize the microscopic origin
319 of the predicted transference numbers, we consider the degree of correlation of the Li^+ and $TFSI^-$
320 displacements at r = 0.1. As detailed in the *Supporting Information*, we find moderate anti-correlated
321 motion and the following picture emerges: at short time scales (i.e. lower than the residence time of Li^+
322 with a polymer segment), the $Li^+(EO)_6$ complex partially diffuses in the direction opposite of the $TFSI^-$ anion
323 somewhat resembling the anticorrelation observed in the tetraglyme-LiTFSI molecular systems [13]. This
324 anticorrelation of the $Li^+(EO)_6$ solvate and $TFSI^-$, which is illustrated in **Figure 5**(c), explains on a microscopic
325 level that t^+ is lower than t^+_{app}. This observation closes the gap between microscopic and macroscopic
326 transport phenomena by suggesting that the lower transference numbers are a result of anticorrelated
327 motion on the nanoscale, which in turn result in significant mass transport of $TFSI^-$ and electrolyte, which
328 then are also anti-correlated.

329

330

331 Conclusions

332

333 We illustrated a novel methodology combining several measurement techniques and simulations to
334 provide quantitative length-scale bridging insight into ion transport in electrolytes. Specifically, we
335 combined synchrotron X-rays to retrieve with high accuracy local electrolyte velocities via XPCS and global
336 concentration gradients via XAM with continuum modelling supported by molecular scale insight provided
337 by MD simulations. To the best of our knowledge, our velocity measurements represent the first spatially
338 resolved direct measurements of ion velocities as a function of time in an electrochemical system. The
339 strength of this approach lies in the opportunity to directly compare physically measured mass transport
340 effects upon cell polarization with those calculated from concentrated solution theory using transport
341 coefficients as input values. Together with MD simulations, this method not only allows us to quantify the
342 transport parameters such as transference number, but also provides atomistic scale insight into the origin
343 of the obtained values. We employed our approach to an exemplar LIB polymeric electrolyte, LiTFSI-PEO,
344 and shed light onto the concentration dependence of the transference numbers in this system, which is
345 debated by researchers; the outlined procedure can also be applied to aqueous and non-aqueous liquid
346 electrolyte when convection can be avoided, as well as to more complex electrolytes, such as composite
347 electrolytes or those infiltrated with fillers for the sake of improved ionic conductivity [51, 52]. Such direct
348 insight paves the way for understanding of ion transport in general, and the proposed methodology can
349 provide novel insight not only into ion transport in polymeric electrolytes but also in liquid electrolyte and

350   electrode materials, as well as separation membranes or polymer electrolyte membranes for fuel cells.
351   Finally, we argue that the many orders increase in coherent flux at diffraction limited storage rings will
352   make probing transport phenomena at microscopic level by XPCS to be applied to other systems taking
353   advantage of the intensity and penetration power of the next generation X-rays beams.
354

369   *Bibliographic references:*
370   1.   E. Gouaux and R. Mackinnon, *Science*, 2005, **310**, 1461-1465.
371   2.   K. Xiao, L. Chen, R. Chen, T. Heil, S. D. C. Lemus, F. Fan, L. Wen, L. Jiang and M. Antonietti, *Nature*
372   *communications*, 2019, **10**, 1-7.
373   3.   K. Xiao, L. Jiang and M. Antonietti, *Joule*, 2019, **3**, 2364-2380.
374   4.   D. Cohen-Tanugi and J. C. Grossman, *Nano letters*, 2012, **12**, 3602-3608.
375   5.   D. T. Hallinan and N. P. Balsara, *Annu. Rev. Mater. Res*, 2013, **43**, 503-525.
376   6.   H. Sun, J. Zhu, D. Baumann, L. Peng, Y. Xu, I. Shakir, Y. Huang and X. Duan, *Nature Reviews*
377   *Materials*, 2019, **4**, 45-60.
378   7.   S. Shi, J. Gao, Y. Liu, Y. Zhao, Q. Wu, W. Ju, C. Ouyang and R. Xiao, *Chinese Physics B*, 2016, **25**.
379   8.   N. P. Balsara and J. Newman, *Journal of The Electrochemical Society*, 2015, **162**, A2720-A2722.
380   9.   J. Newman and K. E. Thomas-Alyea, *Electrochemical systems*, John Wiley & Sons, 2012.
381   10.   I. Villaluenga, D. M. Pesko, K. Timachova, Z. Feng, J. Newman, V. Srinivasan and N. P. Balsara,
382   *Journal of the Electrochemical Society*, 2018, **165**, A2766-A2773.
383   11.   D. J. Brooks, B. V. Merinov, W. A. Goddard, B. Kozinsky and J. Mailoa, *Macromolecules*, 2018, **51**,
384   8987-8995.
385   12.   O. Borodin and G. D. Smith, *Macromolecules*, 2006, **39**, 1620-1629.
386   13.   D. Dong, F. Sälzer, B. Roling and D. Bedrov, *Physical Chemistry Chemical Physics*, 2018, **20**, 29174-
387   29183.
388   14.   K. D. Fong, J. Self, K. M. Diederichsen, B. M. Wood, B. D. Mccloskey and K. A. Persson, *ACS Central*
389   *Science*, 2019, **5**, 1250-1260.
390   15.   D. T. Hallinan, I. Villaluenga and N. P. Balsara, *MRS Bulletin*, 2018, **43**, 759-767.
391   16.   S. B. Aziz, T. J. Woo, M. F. Z. Kadir and H. M. Ahmed, *Journal of Science: Advanced Materials and*
392   *Devices*, 2018, **3**, 1-17.
393   17.   K. M. Diederichsen, E. J. McShane and B. D. McCloskey, *ACS Energy Letters*, 2017, **2**, 2563-2575.
394   18.   M. Doyle, T. F. Fuller and J. Newman, *Electrochimica Acta*, 1994, **39**, 2073-2081.
395   19.   A. Nyman, M. Behm and G. Lindbergh, *Electrochimica Acta*, 2008, **53**, 6356-6365.
396   20.   D. B. Shah, H. K. Kim, H. Q. Nguyen, V. Srinivasan and N. P. Balsara, *The Journal of Physical*
397   *Chemistry C*, 2019, **123**, 23872-23881.
398   21.   M. P. Rosenwinkel and M. Schönhoff, *Journal of The Electrochemical Society*, 2019, **166**, A1977-
399   A1983.
400   22.   J. Evans, C. A. Vincent and P. G. Bruce, *Polymer*, 1987, **28**, 2324-2328.
401   23.   P. G. BRUCE and C. A. VINCENT, *J. Electroanal. Chem.*, 1987, **225**, 1-17.
402   24.   D. M. Pesko, S. Sawhney, J. Newman and N. P. Balsara, *Journal of The Electrochemical Society*,
403   2018, **165**, A3014-A3021.
404   25.   D. M. Pesko, K. Timachova, R. Bhattacharya, M. C. Smith, I. Villaluenga, J. Newman and N. P.
405   Balsara, *Journal of the Electrochemical Society*, 2017, **164**, E3569-E3575.
406   26.   G. Grübel, A. Madsen and A. Robert, *Soft Matter Characterization*, 2008, DOI: 10.1007/978-1-
407   4020-4465-6_13, 953-995.
408   27.   M. Sutton, *Comptes Rendus Physique*, 2008, **9**, 657-667.
409   28.   F. Livet, F. Bley, F. Ehrburger-Dolle, I. Morfin, E. Geissler and M. Sutton, *Journal of Synchrotron*
410   *Radiation*, 2006, **13**, 453-458.
411   29.   B. J. Berne and R. Pecora, *Dynamic light scattering: with applications to chemistry, biology, and*
412   *physics*, Courier Corporation, 2000.
413   30.   F. Ehrburger-Dolle, I. Morfin, F. Bley, F. Livet, G. Heinrich, S. Richter, L. Piché and M. Sutton,
414   *Macromolecules*, 2012, **45**, 8691-8701.
415   31.   J. G. Ulbrandt, M. G. Rainville, C. Wagenbach, S. Narayanan, A. R. Sandy, H. Zhou, K. F. Ludwig and
416   R. L. Headrick, *Nature Physics*, 2016, **12**, 794-799.

417   32.   J. R. M. Lhermitte, M. C. Rogers, S. Manet and M. Sutton, *Review of Scientific Instruments*, 2017,
418   **88**, 0-7.
419   33.   F. Wohde, M. Balabajew and B. Roling, *Journal of The Electrochemical Society*, 2016, **163**, A714-
420   A721.
421   34.   D. M. Pesko, Z. Feng, S. Sawhney, J. Newman, V. Srinivasan and N. P. Balsara, *Journal of The*
422   *Electrochemical Society*, 2018, **165**, A3186-A3194.
423   35.   W. Gorecki, M. Jeannin, E. Belorizky, C. Roux and M. Armand, *Journal of Physics: Condensed*
424   *Matter*, 1995, **7**, 6823-6832.
425   36.   K. Pożyczka, M. Marzantowicz, J. R. Dygas and F. Krok, *Electrochimica Acta*, 2017, **227**, 127-135.
426   37.   C. Xu, B. Sun, T. Gustafsson, K. Edström, D. Brandell and M. Hahlin, *J. Mater. Chem. A*, 2014, **2**,
427   7256-7264.
428   38.   C. F. N. Marchiori, R. P. Carvalho, M. Ebadi, D. Brandell and C. M. Araujo, *Chemistry of Materials*,
429   2020, DOI: 10.1021/acs.chemmater.0c01489.
430   39.   J. Alvarado, M. A. Schroeder, T. P. Pollard, X. Wang, J. Z. Lee, M. Zhang, T. Wynn, M. Ding, O.
431   Borodin, Y. S. Meng and K. Xu, *Energy and Environmental Science*, 2019, **12**, 780-794.
432   40.   H. Yildirim, J. B. Haskins, C. W. Bauschlicher and J. W. Lawson, *The Journal of Physical Chemistry C*,
433   2017, **121**, 28214-28234.
434   41.   I. Rey, J. L. Bruneel, J. Grondin, L. Servant and J. C. Lassegues, *Journal of the Electrochemical*
435   *Society*, 1998, **145**, 3034-3042.
436   42.   C. Brissot, M. Rosso, J. N. Chazalviel and S. Lascaud, *Journal of Power Sources*, 2001, **94**, 212-218.
437   43.   C. Brissot, M. Rosso, J. N. Chazalviel and S. Lascaud, *Journal of the Electrochemical Society*, 1999,
438   **146**, 4393-4400.
439   44.   P. Georén, J. Adebahr, P. Jacobsson and G. Lindbergh, *Journal of The Electrochemical Society*,
440   2002, **149**.
441   45.   J. Newman and T. W. Chapman, *Aiche Journal*, 1973, **19**, 343-348.
442   46.   D. Takamatsu, A. Yoneyama, Y. Asari and T. Hirano, *J Am Chem Soc*, 2018, **140**, 1608-1611.
443   47.   P. Georen and G. Lindbergh, *Electrochimica Acta*, 2001, **47**, 577-587.
444   48.   R. L. Gardas and J. A. P. Coutinho, *Fluid Phase Equilibria*, 2008, **263**, 26-32.
445   49.   N. Molinari, J. P. Mailoa and B. Kozinsky, *Chemistry of Materials*, 2018, **30**, 6298-6306.
446   50.   H.-K. Kim, N. P. Balsara and V. Srinivasan, *Journal of The Electrochemical Society*, 2020, **167**.
447   51.   J.-F. Wu and X. Guo, *Journal of Materials Chemistry A*, 2019, **7**, 2653-2659.
448   52.   W. Tang, S. Tang, X. Guan, X. Zhang, Q. Xiang and J. Luo, *Advanced Functional Materials*, 2019, **29**.
449   53.   A. R. Sandy, L. B. Lurio, S. G. J. Mochrie, A. Malik, G. B. Stephenson, J. F. Pelletier and M. Sutton,
450   *Journal of Synchrotron Radiation*, 1999, **6**, 1174-1184.

451

(a)

XAM: local concentration
CM: local concentration, instantaneous velocity
MD: molecular scale transport

XPCS: instantaneous
local velocity v_{EO}

Li electrode

e^-

V

diffusion

Li$^+$ TFSI$^-$ EO

migration   volume conservation

c_{LiTFSI} c_{PEO}

Li$^0 \leftarrow$ Li$^+$

Li$^+ \leftarrow$ Li^0

electrolyte

(b)

heterodyne XPCS
speckle pattern

transmitted beam detector:
$I_0 e^{-\mu(c_{TFSI})t}$

XAM

EO drifting
with velocity v_{EO}

PEEK window:
heterodyne reference

Li electrode

EO EO EO
EO EO
EO EO

e^-

0.3 V

t autocorrelation

g_2 $\omega \propto v_{EO}$

τ

coherent x-rays

beam rastering
across sample

I_0

15 µm

452
453   **Figure 1:** Conceptualization of the problem and our approach (a) Illustration of mass transport in an
454   electrochemical symmetric cell, in which Li electrodes are separated by an electrolyte made up from
455   ethylene oxide monomers (representing PEO polymer), Li$^+$ cations, and TFSI$^-$ anions. Upon application of an
456   electric field across the cell, Li$^+$ ions migrate in the electric field to the negative electrode, whereas TFSI$^-$
457   ions migrate to the positive electrode (magenta arrows, length of which indicates relative velocities). As Li$^+$
458   is produced at the positive electrode and consumed at the negative electrode (blue arrows), whereas TFSI$^-$

459   ions are blocked, a salt concentration gradient (c_{LiTFSI}, solid line) builds up due to electroneutrality.

460   Consequently, the ions feel a diffusion force towards the negative electrode from the concentration

461   gradient (yellow arrows). When migration and diffusion forces acting upon $TFSI^-$ ions are equal, steady state

462   is reached, and there exists no $TFSI^-$ mass transport. At high salt concentrations, EO monomers are forced

463   to the negative electrode due to mass conservation (green arrows) resulting in a concentration gradient in

464   PEO (c_{PEO}, dashed line). The EO velocity scales with the molar volumes of the salt and EO. The macroscopic

465   concentration gradient is measured by XAM and predicted by our continuum model, whereas our MD

466   simulations unravel the molecular scale transport mechanism. $TFSI^-$ velocities can be directly correlated to

467   the measured EO velocities by XPCS and predicted by our continuum model. (b) Schematic of cell design

468   (technical drawing in Figure S1) and experimental setup to measure EO velocity and $TFSI^-$ concentration

469   profiles at 90 °C; not to scale. The heating setup is neglected for simplicity. The lithium electrodes are

470   separated by 3 mm, and are connected to a potentiostat with a potential of 0.3 V applied between the

471   electrodes. Heterodyne XPCS: The speckle pattern resulting from scattering of a coherent X-ray beam is

472   recorded as a function of time; the beamline producing the coherent X-ray beam is described in Ref. [53]. In

473   the scenario of EO moving at a constant drift velocity, the heterodyne autocorrelation function shows

474   oscillations, the inverse period of which is proportional to the EO velocity. XAM: The transmitted beam

475   intensity is recorded as a function of time. Spatial resolution across the channel is achieved by rastering the

476   15 µm beam across the channel.
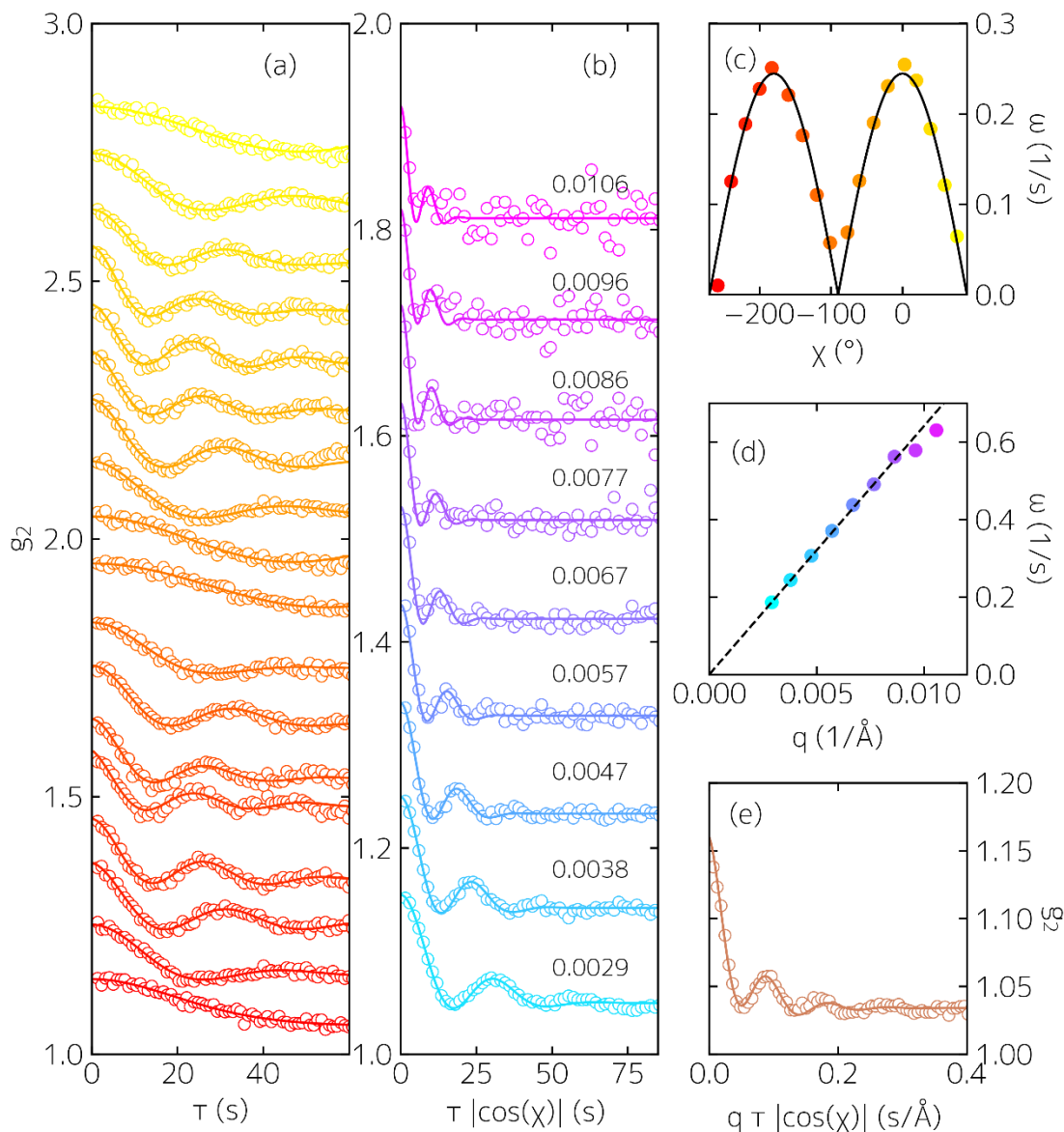
477
478   **Figure 2**: XPCS analysis. (a) Measured auto-correlation functions (markers) as a function of delay time τ for
479   different χ-values at a q-value of 0.0038 Å (corresponding to scattering vectors q within the second
480   innermost ring in Figure S2), and model fits (lines) to Equation 1. The curves are vertically shifted for clarity.
481   (c) Frequency parameters ω derived from fits in (b) (markers) as a function of χ and the fit (line) to
482   Equation 2 (colors correspond to colors in (a)). (b) χ scaled correlation functions (markers) for the first nine
483   q-values (indicated on top of each curve in Å^{-1}) and model fits (lines) to Equation 1. The curves are vertically
484   shifted for clarity. (d) Frequency parameters ω derived from fits in (b) (markers) as a function of q. The line
485   is a guide to the eye showing the expected linear behavior and a zero intercept (colors corresponds to
486   colors in (b)). (e) χ- and q-scaled master correlation function (markers) collapsed from 72 individual
487   correlation function and model fit (line) to Equation 1.
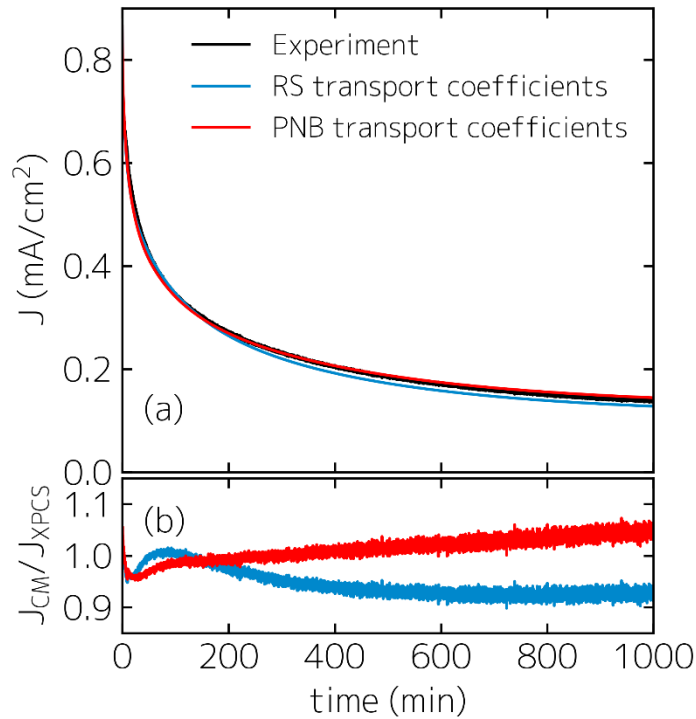
488
489   **Figure 3**: Electrochemistry (a) Experimental current density measured upon constant voltage (0.3 V)
490   polarization of the Li/LiTFSI-PEO/Li symmetric cell of channel length of 3 mm (black line). Continuum model
491   predicted current density under conditions identical to the experiment using *RS transport coefficients* [21]
492   (blue) and *PNB transport coefficients* [25, 34] (red). (b) Continuum model predicted current density (using *RS*
493   *transport coefficients* [21] (blue) and *PNB transport coefficients* [25, 34] (red)) divided by experimental current
494   density.
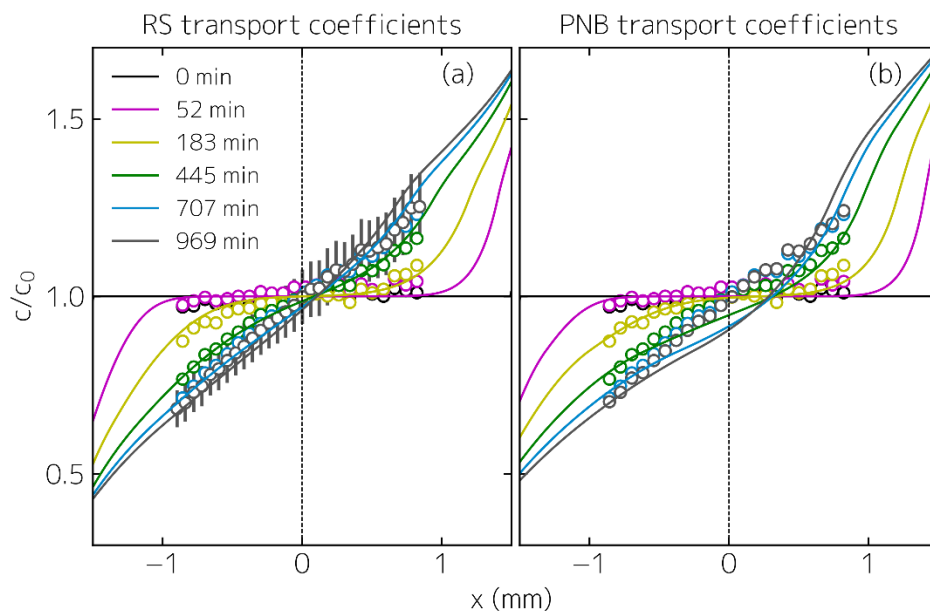
Figure 4: Concentration polarization. (a) Experimental TFSI⁻ concentration (markers) for different times measured upon constant voltage (0.3 V) polarization of the Li/LiTFSI-PEO/Li symmetric cell of channel length of 3 mm, and TFSI⁻ concentration predicted from continuum model under conditions identical to the experiment using *RS transport coefficients* [21] (lines); experimental error-bars are only shown for the curve at 969 min. (b) same as (a) using *PNB transport coefficients* [25, 34].
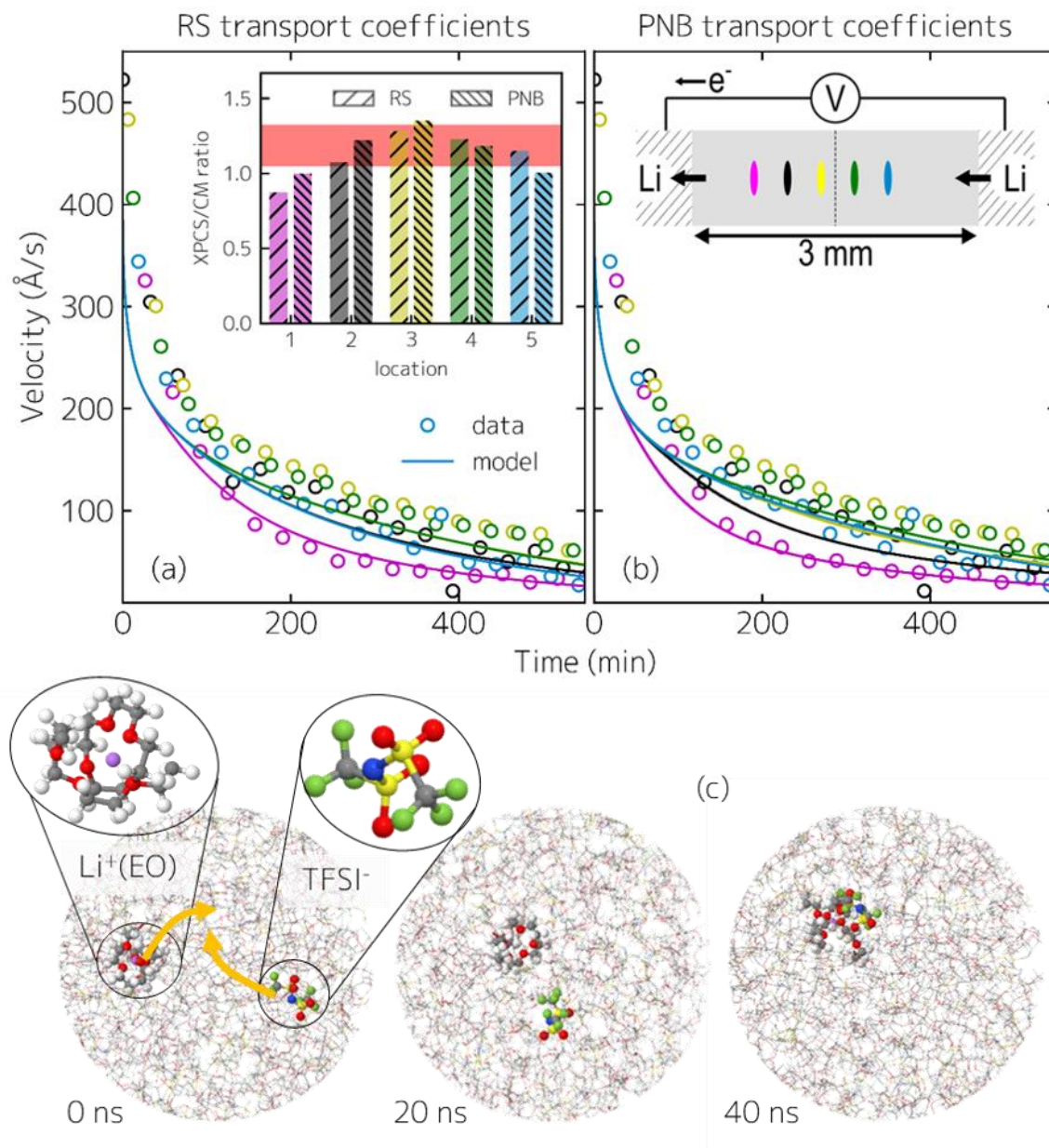
Figure 5: Electrolyte velocities. (a) XPCS-derived TFSI⁻ velocity (markers) for different locations within cell (color-code corresponding to the inset in (b), i.e. x = -0.85 ± 0.04, -0.50 ± 0.04, -0.15 ± 0.04, 0.20 ± 0.04, and 0.55 ± 0.04 mm, where x = 0 corresponds to the half-way point between the electrodes indicated by the dashed line) measured upon constant voltage (0.3 V) polarization of the Li/LiTFSI-PEO/Li symmetric cell of channel length of 3 mm (see inset in (b)) as a function of time, and TFSI velocity predicted from continuum model under conditions identical to the experiment using **RS transport coefficients** [21] (lines). The inset shows the polarization time-averaged (200 < t < 400 min) ratio between the XPCS measured and CM model simulation TFSI velocities for the five different locations. The red bar is centered around the mean ratio (1.19) between experiment and both simulations at the black, yellow, green, and blue locations and has a width of ± 1.5 x the standard deviation of 0.10. (b) same as (a) using **PNB transport coefficients** [25, 34]. The colored regions in the inset correspond to the measured locations in the channel and are color coded with the velocity measurements (markers) and CM predictions (lines). We note that velocities after

514   polarization times greater than about 550 minutes were not resolvable. (c) MD trajectories showing
515   anticorrelation motion (movement towards each other as indicated by the orange arrows) of a
516   representative Li$^+$(EO) complex and TFSI$^-$ (white: H, grey: C, red: O, magenta: Li, green: F, blue: N, yellow:
517   S).